Available online at www.sciencedirect.com
ScienceDirect
Comput. Methods Appl. Mech. Engrg. 366 (2020) 113019
Computer methods in applied mechanics and engineering
www.elsevier.com/locate/cma

Phase field modeling of fracture in Quasi-Brittle materials using natural neighbor Galerkin method

P. Kasirajan[a], S. Bhattacharya[a], A. Rajagopal[a,*], J.N. Reddy[b]

[a] *Indian Institute of Technology Hyderabad, Telangana 5002285, India*
[b] *Texas A&M University, College Station, TX 77845, USA*

Received 4 May 2019; received in revised form 18 March 2020; accepted 19 March 2020
Available online xxxx

Abstract

Recently developed phase field models of fracture require a diffusive crack representation based on an introduction of a crack phase field. We outline a thermodynamically consistent framework for phase field models of crack propagation in elastic solids, develop incremental variational principles. In this work, the numerical implementation of the phase field model for brittle fracture using natural neighbor Galerkin method is presented. Phase field method diffuses the sharp discontinuity by introducing a regularized crack functional. The notion of regularized crack functional provides a basis for defining suitable convex dissipation functions which govern the evolution of the crack phase field. The use of natural neighbors to dynamically decide the compact support at a nodal point makes it truly mesh free and nonlocal. The method uses smooth non-polynomial type Sibson interpolants, which are C^0 at a given node and C^∞ everywhere else. This allows to capture the interface region in a phase field model more accurately with only few nodes. For a given accuracy, there is an improvement in the computational time with the use of natural neighbor interpolants. Several benchmark problems were solved to investigate the efficiency of the numerical implementation of phase field model using natural neighbor Galerkin method.

Keywords: Phase field; Fracture; Quasi brittle material; Natural neighbor Galerkin method

1. Introduction

One of the most common failure modes encountered in engineering materials is fracture. A major interest in designing engineering structures has been to prevent cracking induced failures. Similar to many other physical localization phenomena, the computational modeling of nucleation, growth, and propagation of cracks in engineering materials has been important to comprehend the failure mechanisms. In the field of brittle fracture mechanics, the pioneering work of Griffith [1] has given the direction, followed by notable works from Irwin [2] and Rice [3]. Griffith's approach is based on the global energy minimization of a cracking solid. Among various approaches of modeling crack propagation, the continuous (smeared) approaches [4] based on continuum damage mechanics (CDM) [5] and the discontinuous (discrete) cohesive zone models (CZM) [6] and [7] are popularly adopted. Discrete

* Corresponding author.
E-mail address: rajagopal@iith.ac.in (A. Rajagopal).

https://doi.org/10.1016/j.cma.2020.113019

models use various techniques such as remeshing, interface elements, and XFEM [8] to resolve the crack front. On the other hand, smeared models cease to give meaningful results when the material undergoes softening [9] and [10].

In discrete crack models, displacements are discontinuous across geometrically sharp crack interfaces. The singular strain field has intensity depending on the orientation of the crack [11] and the displacement jump [12]. There is a need to accurately represent the displacement jump [13] and track the progression of the crack [14]. To accurately represent the fracture, there is a need for two material models: (1) model for the bulk material as elastic with embedded cracks [15] or with damage based models [16] and (2) model for treating the crack as a cohesive interface defined by a traction separation law [17]. The cohesive models, however, require specification of initial penalty in stiffness to avoid interpenetration of the crack surfaces upon contact. Subsequent to these approaches, to over come the problems of singularity and jumps in displacement fields, regularization approaches that consider a uniform or non-uniform spread of the nonlinear singular strain fields over a localized region [18] of finite width [19]. The size of the regularization region is related to the mesh size. In approaches used to model strong discontinuities, the bandwidth is chosen as small as possible to reach the sharp interface limits in a limiting sense. Such approaches have been combined with regularized XFEM to achieve the singularity of the displacement field at the crack tip [20].

In smeared or continuous crack models, the displacement field is continuous, resulting in uniform strain field. The models based on continuum damage mechanics concepts are mostly adopted [21] in local approaches. However, these models cease to give meaningful results when the material undergoes softening (see [9] and [10]). This leads to loss of ellipticity of the mathematical problem. To circumvent this, generalized continuum models such as nonlocal damage models [22] and gradient damage models [23–27] and [28] are adopted [24]. The crack driving force is defined either in an integral form [9] or in a gradient form [29] and [30] together with the boundary or surface effects [31]. The gradient damage models have been implemented in the commercial finite element package (ABAQUS) [32]. The nonlocal models use a diffusive crack to circumvent the problem of tracking the interface. However, if the diffused description is not accurate and does not converge to the sharp interface limit asymptotically, the predicted behavior of the crack nucleation and propagation becomes incorrect and leads to the loss of ellipticity of the mechanical equilibrium equations. Modifications such as homogenized local gradient damage model with micro inertia effects and the stress-based nonlocal models have been recently been proposed to make the method more efficient [33]. Continuum Damage Mechanics based methodology for high cycle fatigue crack growth simulations have been developed and implemented in the framework of extended finite element method in the work of Pandey et al. [34].

Phase field approaches are synonymous to the smeared or diffused crack approaches and primarily deal with geometrical regularization of the cracking body (see, e.g., [35–45] and [46]). In a phase field model, the evolution of a crack front is directly obtained from the solution of coupled governing equations describing the evolution of the crack phase field and mechanical equilibrium. The method has a continuous displacement field together with a regular strain field. A stress–strain relationship in terms of the damage is enough to model the overall nonlinear behavior of the cracking body. The evolution of the damage is derived from the energy minimization condition. There has been recent focus in the application of this method for cohesive fracture (see [45] and [46]). The method has been applied to brittle and quasi-brittle fracture (see [47] and [48]). In contrast to discrete fracture models, there is no need of using sophisticated algorithms to track the fracture surface in phase field models.

A typical phase field model invokes the calculus of variations to derive the equilibrium equations by minimizing the total energy of the system. Francfort et al. [49] first proposed the brittle fracture problem as an energy minimization which can be viewed as the generalization of Griffith's theory of LEFM. The problem of crack nucleation and its propagation has been solved in a variational setting. The length scale is regarded as a material property, it is a numerical parameter of which value can be taken as small as possible. For very small values of chosen length scale the phase field model tends towards cohesive zone model in the limit [47].

Though there are many applications of phase field method for modeling brittle fracture, only a few employed it for modeling ductile fracture in solids. Ambati et al. [50] proposed a novel model to bring in the effect of ductility in elasto-plastic solids in the quasi-static kinematically linear regime. This proposed model also agrees well with the experimental results. Kuhn et al. [51] proposed a phase field model for ductile fracture that can decouple the plastic material law and fracture phase field which is advantageous from numerical point of view. Hence the governing equations can be solved monolithically. Borden et al. [36] for the first time investigated the effects of stress triaxiality on ductile fracture. They used a cubic degradation function unlike a quadratic degradation function found in literature and a mechanism for the plastic softening by introducing a yield surface degradation function etc.

Phase field models are also employed in dynamic setting [52,53] and [54] and the finite strain setting (see [35,43] and [37]). Since the phase field description does not require any additional criterion to track the crack propagation, the complex crack topologies such as branching and merging can be easily dealt even in three dimensions. Lee et al. [55] studied the fracture propagation in porous media by demonstrating an efficient algorithm that can save computational time for 3D applications. Borden et al. [56] presented a fourth order approximation to the crack surface in contrast to the standard second order approximation of Bourdin et al. [57]. The proposed model has also been demonstrated to study the crack propagation in three dimensions. Pham et al. [42] developed a three dimensional finite element code for the phase field brittle fracture modeling and validated their results with that of experimental results under mixed mode conditions.

Griffith's brittle fracture model assumes that fracture energy dissipates at the instant of crack nucleation where as in cohesive fracture models the fracture energy depends on the extension of the crack opening. The regularized variational formulation in the context of cohesive fracture has been developed by Alessi et al. [58]. The phase field method has been applied to model fracture in plates and shells [37,59,60] and [61]. There is a recent trend on using enriched finite element approximations like in XFEM for analysis of phase field problems [62], to get better approximations near the crack tip. Modeling dynamic fracture of solids with a phase-field regularized cohesive zone model [46] has also been a recent advance. Patil et al. proposed a new multiscale phase field method to simulate crack propagation in composites [63] and a local moving extended phase field method (LMXPFM) for the failure analysis of brittle materials [64].

Any numerical strategy for the implementation of the phase field model should address the issue of the smoothness of approximation required to accurately capture the distribution of the phase field parameter over the regularized region defined by a suitable limiting length scale parameter. In a limiting sense, the diffused interface model must reduce to sharp interface model at very low values of the length scale. There has been some recent works on use of mesh less methods for implementation of phase field models of fracture. For instance Element free Galerkin method [65], consistent mesh less method [66] have been proposed. In the present work, we aim to address the issues related to the need of finer mesh near the crack path and accuracy of the solution. Therefore, we use a mesh free natural neighbor Galerkin method for phase field modeling of the fracture problems. The notion of use of natural neighbors to dynamically decide the compact support at a nodal point renders it truly mesh free and nonlocal. The method uses smooth non-polynomial type Sibson interpolants, which are C^0 at a given node and C^∞ every where. This allows accurate capture of the interface region in a phase field model with only fewer nodes compared to the standard finite element method. Further, we do not need to implement any adaptive strategy like in mesh based methods. This may be attributed to the fact that the Natural Neighbor Galerkin method shape functions are very smooth and higher order continuous. Although an adaptive strategy with NNGM will improve the computational time, in the present study, the interest is to consider only this aspect of very smooth approximation functions of the method and study the performance of the NNGM method with uniform refinements for various grid sizes without an adaptive approach.For a required accuracy, the cost of computation from the natural neighbor Galerkin method is almost equal to the finite element method. For the same quadrature, the mesh free method gives more accurate results.

The paper is arranged as follows. In Section 2, the phase field model for brittle fracture is presented. This is followed by a discussion on natural neighbor Galerkin method in Section 3. Numerical implementation including the staggered solution approach is discussed in Section 4. In the last section some numerical examples are presented to illustrate the benefits from the present approach.

2. Phase field model for brittle fracture

Let us consider a continuous body $\mathcal{B} \in \mathbb{R}^\delta (\delta \in 1, 2, 3)$ with the sharp crack $\Gamma \in \mathbb{R}^{\delta-1}$ as shown in Fig. 1. Let $\boldsymbol{u}(\boldsymbol{x}, t)$ be the displacement of any material point at $\boldsymbol{x} \in \mathcal{B}$ at any time $t \in \mathbb{R}$. Consider $\boldsymbol{b}$ as the body force field per unit volume and $\boldsymbol{t}$ as the tractions on the boundary $\partial\mathcal{B}_t$. In 1920, Griffith [1] laid out the theoretical foundation for brittle fracture. Griffith's theory suffers from limitations such as the inability to predict crack nucleation and identify complex crack paths. These limitations are overcome by the variational framework of Griffith's theory introduced by Francfort et al. [49]. The process of crack initiation and propagation in the body is governed by the minimization of the total energy functional written as

$$\mathcal{E}(\boldsymbol{u}, \Gamma) = \mathsf{E}_s + \mathsf{E}_f - \mathsf{P} \tag{1}$$

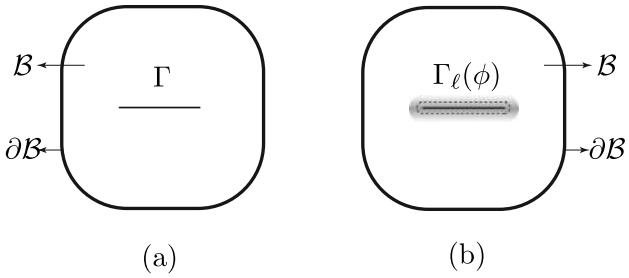

Fig. 1. (a) Sharp crack Γ embedded in the body $\mathcal{B}$ and (b) Regularized crack surface Γ_ℓ.

E_S, E_f and P are the strain energy, fracture energy and energy due to external forces written as

$$\mathsf{E}_s = \int_{\mathcal{B}} \psi_0(\boldsymbol{\varepsilon})\, dV, \quad \mathsf{E}_f = \int_{\Gamma} G_c\, dA, \quad \mathsf{P} = \int_{\mathcal{B}} \boldsymbol{b}\cdot\boldsymbol{u}\, dV + \int_{\partial\mathcal{B}} \boldsymbol{t}\cdot\boldsymbol{u}\, dA \tag{2}$$

ψ_0 is the elastic energy density and G_c, a material parameter known as Griffith's critical energy release rate, is the energy required to create two new fracture surfaces. This minimization problem is referred to as a free discontinuity problem [67]. It should be noted that the crack path Γ and the displacement field $\boldsymbol{u}$ (discontinuous across Γ) are not known a priori.

2.1. Phase field approximation for a sharp crack

We implement the free discontinuity problem by introducing a phase field $\phi(\boldsymbol{x}, t)$ for the description of a sharp crack Γ in a solid continuum $\mathcal{B}$. Its value at any material point varies between 0 and 1 ($\phi = 0$ and $\phi = 1$ representing undamaged and fully damaged phases, respectively). The phase field $\phi(\boldsymbol{x}, t)$ captures the onset and development of micro-voids and micro-cracks in a macroscopically homogeneous body. Bourdin et al. [57] presented the regularized variational framework of Griffith's theory to study the diffused crack propagation. The sharp crack Γ is regularized with the functional Γ_ℓ as

$$\Gamma_\ell = \int_{\mathcal{B}} \gamma(\phi, \nabla\phi)\, dV, \quad \gamma(\phi, \nabla\phi) = \frac{1}{2\ell}\left(\phi^2 + \ell^2 |\nabla\phi|^2\right) \tag{3}$$

where, $\gamma(\phi, \nabla\phi)$ is the crack surface energy density function per unit volume of the solid as given by Miehe et al. [53]. The length scale ℓ governs the width of the crack, i.e., it governs the region where ϕ transitions from 1 to 0. It is to be noted that for vanishing length scales $\ell \to 0$, the regularized crack functional Γ_ℓ converges to the sharp crack Γ ($\Gamma_\ell \to \Gamma$). For any sharp crack Γ in the body, the regularized crack phase field $\phi(\boldsymbol{x})$ can be obtained by minimizing the functional Γ_ℓ with respect to ϕ, subject to the Dirichlet type condition $\phi = 1$ on the sharp crack Γ. The Euler equations for the minimization problem are given as $\phi - \ell^2 \triangle \phi = 0$ along with the Neumann type boundary condition $\nabla\phi \cdot \boldsymbol{n} = 0$ on $\partial\mathcal{B}$. This is demonstrated using a numerical example in Section 5.2. Using the crack surface density function $\gamma(\phi, \nabla\phi)$ given in Eq. (3), the fracture energy E_f can now be written as

$$\mathsf{E}_f = \int_{\Gamma} G_c\, dA = \int_{\mathcal{B}} G_c \gamma(\phi, \nabla\phi)\, dV \tag{4}$$

2.2. Governing equations

Since the phase field $\phi(\boldsymbol{x}, t)$ is smeared, the degradation of the elastic energy density with increase in the phase field should be accounted for. Therefore, the strain energy of the body is written as

$$\mathsf{E}_s = \int_{\mathcal{B}} \left[(1-\phi)^2 + \mathsf{k}\right] \psi_0(\boldsymbol{\varepsilon})\, dV, \quad \psi_0(\boldsymbol{\varepsilon}) = \frac{1}{2}\lambda\ \mathrm{tr}^2(\boldsymbol{\varepsilon}) + \mu\ \mathrm{tr}(\boldsymbol{\varepsilon}^2) \tag{5}$$

where, λ and μ are Lame's constants. k is a small positive constant which ensures a small artificial stiffness of $\mathsf{k}\psi_0(\boldsymbol{\varepsilon})$ at a fully broken state of $\phi(\boldsymbol{x}, t) = 1$. The expression for strain energy of the body as written in Eq. (5) facilitates crack growth under compression, which is an unrealistic response. To ensure the crack growth only under

tension, only tensile part of the elastic energy should be degraded with the increase in the phase field. Therefore, the strain energy of the body is given as

$$\mathsf{E}_s = \int_{\mathcal{B}} \left[(1-\phi)^2 + \mathsf{k}\right] \psi_0^+(\boldsymbol{\varepsilon})\, dV + \int_{\mathcal{B}} \psi_0^-(\boldsymbol{\varepsilon})\, dV \tag{6}$$

ψ_0^+ and ψ_0^- are defined as given by Miehe et al. [53] on the basis of the spectral decomposition of the strain tensor as $\boldsymbol{\varepsilon} = \sum_{i=1}^{\delta} \varepsilon^i \boldsymbol{n}^i \otimes \boldsymbol{n}^i$, where ε^i and $\boldsymbol{n}^i$ are principal strains and principal strain directions. Using this, we write $\boldsymbol{\varepsilon}_\pm = \sum_{i=1}^{\delta} \langle \varepsilon^i \rangle_\pm \boldsymbol{n}^i \otimes \boldsymbol{n}^i$ along with the definition $\langle a \rangle_\pm = \frac{(a \pm |a|)}{2}$. Then, the tensile and compressive part of the energy are given by

$$\psi_0^\pm(\boldsymbol{\varepsilon}) = \frac{1}{2}\lambda \langle \mathrm{tr}(\boldsymbol{\varepsilon}) \rangle_\pm^2 + \mu\, \mathrm{tr}(\boldsymbol{\varepsilon}_\pm^2) \tag{7}$$

Using the expressions of the strain energy of the body from Eq. (6) and the fracture energy from Eq. (4), the total energy functional in Eq. (1) can be rewritten as given by

$$\mathcal{E}(\boldsymbol{u}, \phi) = \int_{\mathcal{B}} \left[(1-\phi)^2 + \mathsf{k}\right] \psi_0^+(\boldsymbol{\varepsilon})\, dV + \int_{\mathcal{B}} \psi_0^-(\boldsymbol{\varepsilon})\, dV + \int_{\mathcal{B}} G_c \gamma(\phi, \nabla\phi)\, dV - \int_{\mathcal{B}} \boldsymbol{b} \cdot \boldsymbol{u}\, dV - \int_{\partial\mathcal{B}} \boldsymbol{t} \cdot \boldsymbol{u}\, dA \tag{8}$$

Minimizing the total energy functional $\mathcal{E}(\boldsymbol{u}, \phi)$ results in the coupled evolution equations for the displacement field $\boldsymbol{u}$ and the phase field ϕ written as follows

$$\nabla \cdot \left\{ \left[(1-\phi)^2 + \mathsf{k}\right] \partial_{\boldsymbol{\varepsilon}} \psi_0^+ + \partial_{\boldsymbol{\varepsilon}} \psi_0^- \right\} + \boldsymbol{b} = 0 \tag{9}$$

$$\left(\frac{1}{\ell} + 2\frac{\psi_0^+}{G_c} \right) \phi - \ell \nabla^2 \phi = 2\frac{\psi_0^+}{G_c} \tag{10}$$

along with the Newmann type boundary conditions

$$\boldsymbol{\sigma} \cdot \boldsymbol{n} = \boldsymbol{t} \quad (\text{on } \partial\mathcal{B}_t) \qquad \text{and} \qquad \nabla\phi \cdot \boldsymbol{n} = 0 \quad (\text{on } \partial\mathcal{B}) \tag{11}$$

It should be noted that the tensile part of the elastic energy ψ_0^+ drives the evolution of the phase field ϕ. However, the form of Eq. (10) does not ensure that the phase field is monotonically increasing in the loading history. To enforce the irreversibility of the phase field, a history parameter H was introduced in the work of Miehe et al. [53]. The history parameter represents the maximum value of tensile part of the elastic energy in the loading history:

$$\mathsf{H}(\boldsymbol{x}, t) = \max_{t \in [0,T]} \psi_0^+(\boldsymbol{\varepsilon}) \tag{12}$$

Replacing the term $\psi_0^+(\boldsymbol{\varepsilon})$ in Eq. (10) with the history parameter H, we can rewrite the evolution equation of the phase field as

$$\left(\frac{1}{\ell} + \frac{2\mathsf{H}}{G_c} \right) \phi - \ell \nabla^2 \phi = \frac{2\mathsf{H}}{G_c} \tag{13}$$

2.3. Hybrid model

We have two primary field variables: the displacement field $\boldsymbol{u}(\boldsymbol{x}, t)$ and the phase field $\phi(\boldsymbol{x}, t)$. The strong form of the evolution equations for these two fields are given as

$$\nabla \cdot \left\{ \left[(1-\phi)^2 + \mathsf{k}\right] \partial_{\boldsymbol{\varepsilon}} \psi_0^+ + \partial_{\boldsymbol{\varepsilon}} \psi_0^- \right\} + \boldsymbol{b} = 0 \tag{14a}$$

$$\left(\frac{1}{\ell} + \frac{2\mathsf{H}}{G_c} \right) \phi - \ell \nabla^2 \phi = \frac{2\mathsf{H}}{G_c} \tag{14b}$$

The introduction of the history parameter H decouples the above equations and enables us to solve them using a robust staggered scheme. However, because of the elastic energy density split in (6), Eq. (14a) is nonlinear which

results in higher computational cost. To overcome this issue, a hybrid model which uses linear momentum balance equation but still ensures that the tensile part of the elastic energy density $\psi_0^+(\boldsymbol{\varepsilon})$ drives the phase field ϕ. The strong form of the evolution equations can be rewritten as

$$\nabla \cdot \left\{ \left[(1-\phi)^2 + \mathsf{k} \right] \partial_{\boldsymbol{\varepsilon}} \psi_0 \right\} + \boldsymbol{b} = 0 \tag{15a}$$

$$\left(\frac{1}{\ell} + \frac{2\mathsf{H}}{G_c} \right) \phi - \ell \nabla^2 \phi = \frac{2\mathsf{H}}{G_c} \tag{15b}$$

with the definition for the history parameter H in (12) still the same. Also, at any point $\boldsymbol{x}$ when $\psi_0^+ < \psi_0^-$, the phase field ϕ should be set as zero to prevent the crack surface interpenetration. Also, the evolution equation of the phase field ϕ can be recast into the Ginzburg–Landau type equation with a viscosity parameter η as

$$\eta \dot{\phi} = \partial_\phi \mathcal{E} \tag{16}$$

which leads to the modified form of evolution equations written as

$$\nabla \cdot \left\{ \left[(1-\phi)^2 + \mathsf{k} \right] \partial_{\boldsymbol{\varepsilon}} \psi_0 \right\} + \boldsymbol{b} = 0 \tag{17a}$$

$$\left(\frac{1}{\ell} + \frac{2\mathsf{H}}{G_c} \right) \phi - \ell \nabla^2 \phi + \eta \dot{\phi} = \frac{2\mathsf{H}}{G_c} \tag{17b}$$

The general idea in devising the hybrid model was to retain a linear momentum balance equation within a staggered scheme, in order to keep a computational cost comparable to that of the isotropic model. This results in retaining Eq. (15a) from the isotropic model. However, the evolution of ϕ should be driven merely by the tensile part of the elastic energy ψ_0^+ to avoid cracking in the compressed regions. This motivates keeping Eq. (15b), in which the definition for the history parameter is $\mathsf{H} = \max_{t \in [0,T]} \psi_0^+(\boldsymbol{\varepsilon})$. Also, to prevent the crack surface interpenetration, at any point $\boldsymbol{x}$ when $\psi_0^+ < \psi_0^-$, the phase field ϕ should be set as zero [50].

3. Natural neighbor Galerkin method

Natural neighbor Galerkin method is a mesh less numerical tool for solving the partial differential equations. Like any meshless method, it does not require fixed connectivity information between nodes. In this section, the application of natural neighbor Galerkin method to solve the phase field equations is presented.

Let us consider a plane in $\mathbb{R}^2$ consisting of a set of distinct nodal points as shown in Fig. 2. The construction of trial and test functions are based on natural neighbor interpolation. Natural neighbor interpolants are constructed on the basis of the Voronoi tessellation of the domain with scattered nodal points. The Voronoi tessellation partitions the plane into domains associated with each node such that any point in that domain is closer to the nodal point it is associated with than any other node in the plane. These domains are called Voronoi or Thiessen polygons. The Voronoi tessellation is unique for a nodal set. Mathematically, Voronoi polygon associated with any node P_I is written as

$$V_I = \{ \boldsymbol{x} \in \mathbb{R}^2 : \ d(\boldsymbol{x}, P_I) < d(\boldsymbol{x}, P_J), \quad \forall J \neq I \} \tag{18}$$

where, $d(\boldsymbol{x}, P_I)$, the Euclidean metric, is the distance between $\boldsymbol{x}$ and P_I. Any two nodes sharing a common Voronoi edge are called natural neighbors.

Delaunay triangulation of a nodal set is constructed by joining all the natural neighbors. The significance of the Delaunay triangles in this approach is that they are used as the background cells for numerical integration. One of the important property of Delaunay triangles is the empty circumcircle criterion: the circumcircle of a Delaunay triangle contains no other nodes except the three nodes that form the vertex of that Delaunay triangle. This criterion is employed in finding the nodes that are natural neighbors to any quadrature point. Voronoi Tessellation and Delaunay triangulation of a nodal point set are dual to each other. Voronoi tessellation and Delaunay triangulation for a nodal point set is given pictorially in Fig. 2a and 2b, respectively.

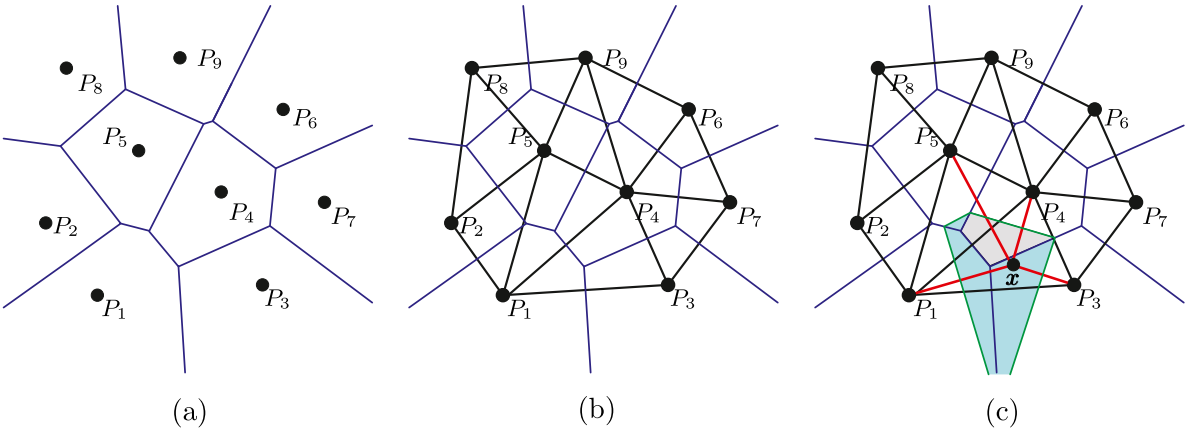

Fig. 2. (a) Voronoi diagram of a nodal set, (b) Delaunay triangulation, and (c) Second order Voronoi polygon for $\boldsymbol{x}$ in the nodal set, indicating the pictorial representation of the shape function computation.

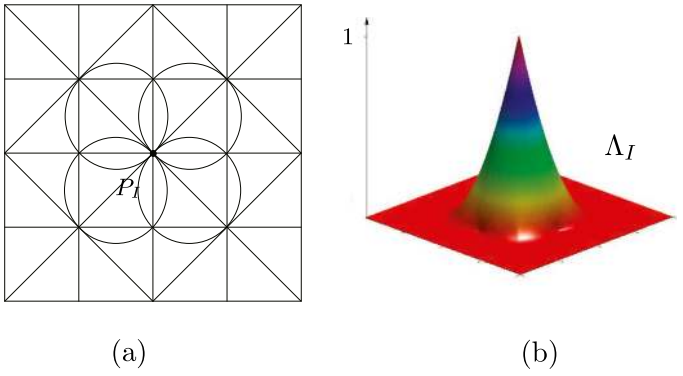

Fig. 3. (a) Support domain for Λ_I related to the node I. (b) Sibson Interpolant Λ_I.

A point $\boldsymbol{x}$ is introduced in the plane consisting of the nodal points at which the natural neighbor interpolant is to be constructed. Empty circumcircle criterion is used to find all the neighbors for the point $\boldsymbol{x}$. The perpendicular bisectors of all the lines joining the point $\boldsymbol{x}$ with its neighbors will form a Voronoi cell corresponding to $\boldsymbol{x}$ (i.e., $V_{\boldsymbol{x}}$). The construction of the natural neighbor interpolant at the point $\boldsymbol{x}$ is based on the definition of second order Voronoi polygon $V_{\boldsymbol{x}I}$. Mathematically, this second order Voronoi polygon corresponding to $\boldsymbol{x}$ is written as,

$$V_{\boldsymbol{x}I} = \{\boldsymbol{x} \in \mathbb{R}^2 : \ d(\boldsymbol{x}, P_I) < d(\boldsymbol{x}, P_J) < d(\boldsymbol{x}, P_K), \quad \forall K \neq I, J\} \tag{19}$$

This second order Voronoi polygon $V_{\boldsymbol{x}I}$ contains all the points that have P_I as the closest node and P_J as the second closest node. The C^0-continuous natural neighbor interpolant $\Lambda_I(\boldsymbol{x})$ with respect to node I evaluated at the point $\boldsymbol{x}$ is defined as the ratio of the area of $V_{\boldsymbol{x}I}$ to the area $V_{\boldsymbol{x}}$. Let us take $\kappa_I(\boldsymbol{x})$ and $\kappa(\boldsymbol{x})$ as the Lebesgue measures of $V_{\boldsymbol{x}I}$ and $V_{\boldsymbol{x}}$, respectively. Then, $\Lambda_I(\boldsymbol{x})$ is given as

$$\Lambda_I(\boldsymbol{x}) = \frac{\kappa_I(\boldsymbol{x})}{\kappa(\boldsymbol{x})} \tag{20}$$

Fig. 2c illustrates how the natural neighbor interpolant is constructed at point $\boldsymbol{x}$ for the node P_4. It is the ratio of the area shaded in gray to the combined area shaded in gray and blue. By the definition of natural neighbor interpolant, it is evident that it is always positive and possess the property of partition of unity. It is also interpolatory in nature and therefore imposition of essential boundary condition can be direct. Natural neighbor interpolants form a partition of unity. They also possess the property of linear completeness. They are C^∞ everywhere except at nodes

where they are C^0. The natural neighbor interpolant corresponding to a node has compact support (i.e., it has non zero values in the region formed by the overlapping of all circumcircles passing through that node). This is shown pictorially in (Fig. 3a). A more detailed description on the implementation of the natural neighbor Galerkin method can be found in [68] and in [69]. The application to other problems can be found in [70] and [71].

4. Numerical implementation

4.1. Weak form and spacial discretization

The weak form of the governing equations (17) is obtained by multiplication with the weight functions (w^u and w^ϕ) and integrating over the body $\mathcal{B}$ as

$$\int_{\mathcal{B}} w^u \left\{ \nabla \cdot \left\{ \left[(1-\phi)^2 + \mathsf{k} \right] \partial_{\boldsymbol{\varepsilon}} \psi_0 \right\} + \boldsymbol{b} \right\} dV = 0 \tag{21a}$$

$$\int_{\mathcal{B}} w^\phi \left\{ \left(\frac{1}{\ell} + \frac{2\mathsf{H}}{G_c} \right) \phi - \ell \nabla^2 \phi + \eta \dot{\phi} - \frac{2\mathsf{H}}{G_c} \right\} dV = 0 \tag{21b}$$

Assuming constant time intervals, we take $\tau = t_{n+1} - t_n$. The rate of the fracture field $\dot{\phi}$ at any time step t_{n+1} is defined as

$$\dot{\phi} = \frac{\phi_{n+1} - \phi_n}{\tau} \tag{22}$$

In the following equations, the primary fields without any time subscripts are considered to be evaluated at the time step t_{n+1}. The displacement field $\boldsymbol{u}(\boldsymbol{x}, t)$ and the phase field $\phi(\boldsymbol{x}, t)$ are approximated using natural neighbor interpolations as

$$\boldsymbol{u}(\boldsymbol{x}, t) = \sum_{I=1}^{N} \Lambda_I(\boldsymbol{x}) \boldsymbol{u}_I(t), \quad \phi(\boldsymbol{x}, t) = \sum_{I=1}^{N} \Lambda_I(\boldsymbol{x}) \phi_I(t) \tag{23}$$

where, N is the total number of nodes used to discretize the body. It is to be noted that $\Lambda_I(\boldsymbol{x})$ has non zero values only in the region formed by the overlapping of circumcicles passing through the node P_I and is zero elsewhere (refer Fig. 3a). Using Galerkin weighted residual method, we choose the natural neighbor interpolants as the weight functions. Thus, from Eq. (21a), we obtain a set of linear algebraic equations as

$$\boldsymbol{K}^u_{IJ}\, \boldsymbol{u}_J = \boldsymbol{f}^u_I \tag{24}$$

where,

$$\boldsymbol{K}^u_{IJ} = \int_{\mathcal{B}} \left[(1-\phi)^2 + \mathsf{k} \right] (\boldsymbol{B}^u)^T_I \boldsymbol{\mathcal{C}} (\boldsymbol{B}^u)_J \, dV, \quad \boldsymbol{f}^u_I = \int_{\mathcal{B}} (\boldsymbol{B}^u)^T_I \boldsymbol{b} \, dV + \int_{\partial\mathcal{B}} (\boldsymbol{B}^u)^T_I \boldsymbol{t} \, dA \tag{25}$$

$\boldsymbol{\mathcal{C}}$ is the plane strain constitutive matrix for linear isotropic material and $\boldsymbol{B}^u$ contains interpolant derivatives written as

$$(\boldsymbol{B}^u)_I = \begin{bmatrix} \Lambda_{I,x} & 0 \\ 0 & \Lambda_{I,y} \\ \Lambda_{I,y} & \Lambda_{I,x} \end{bmatrix} \tag{26}$$

Again, using the natural neighbor interpolants for the weight function w^ϕ in Eq. (21b), we obtain a set of linear algebraic equations as follows

$$\boldsymbol{K}^\phi_{IJ}\, \phi_J = \boldsymbol{f}^\phi_I \tag{27}$$

where,

$$\boldsymbol{K}^\phi_{IJ} = \int_{\mathcal{B}} (\boldsymbol{B}^\phi)^T_I \boldsymbol{\mathcal{D}} (\boldsymbol{B}^\phi)_J \, dV, \quad \boldsymbol{f}^u_I = \int_{\mathcal{B}} (\boldsymbol{B}^\phi)^T_I \boldsymbol{p} \, dV \tag{28}$$

$$\mathcal{D} = \begin{bmatrix} \left(\frac{1}{\ell} + \frac{2\mathsf{H}}{G_c} + \frac{\eta}{\tau}\right) & 0 & 0 \\ 0 & \ell & 0 \\ 0 & 0 & \ell \end{bmatrix}, \quad (\boldsymbol{B}^{\phi})_I = \begin{bmatrix} \Lambda_I \\ \Lambda_{I,x} \\ \Lambda_{I,y} \end{bmatrix}, \quad \boldsymbol{p} = \begin{bmatrix} \frac{2\mathsf{H}}{G_c} + \frac{\eta\phi_n}{\tau} \\ 0 \\ 0 \end{bmatrix} \tag{29}$$

Due to the absence of an element structure in Natural Neighbor Galerkin Method, the stiffness matrices and the force vectors are assembled on the nodal basis in the global level. The stiffness matrix (or force vector) evaluated at every quadrature point are summed up to obtain the global stiffness matrix (or global force vector).

4.2. Staggered algorithm

The subsequent discussion will be about the staggered solution scheme used to solve the governing equations for $\boldsymbol{u}_{t_{n+1}}$ and $\phi_{t_{n+1}}$ at any time step t_{n+1}. The displacement field $\boldsymbol{u}_{t_n}$, the phase field ϕ_{t_n} and the history parameter H_{t_n} are known from the previous time step t_n. At first, the weak form of momentum balance equation (24) is solved for $\boldsymbol{u}_{t_{n+1}}$ using the frozen phase field $\phi = \phi_{t_n}$. Then, using Eq. (12), the history parameter $\mathsf{H}_{t_{n+1}}$ is evaluated at the quadrature points using the displacement field $\boldsymbol{u}_{t_{n+1}}$. Next, the phase field $\phi_{t_{n+1}}$ is solved using Eq. (27) for $\mathsf{H} = \mathsf{H}_{t_{n+1}}$. Finally, the values of $\boldsymbol{u}_{t_{n+1}}$, $\mathsf{H}_{t_{n+1}}$ and $\phi_{t_{n+1}}$ are then stored for the next time step.

5. Numerical examples

In this section, we study the numerical efficiency of our phase field fracture model. The numerical computation was carried out using the natural neighbor shape functions described in Section 3. In all examples, a 3×3 quadrature rule was used for numerical integration over Delaunay triangles. The state of plane strain is considered. Pre-existing notch or crack is used to initiate crack in the numerical examples discussed below. Pre-existing notch is modeled as a discrete one in the geometry in few examples. In other examples, pre-existing crack is induced using the history field H as given in the work of Borden et al. [52]. The history field is set as follows:

$$\mathsf{H}(\boldsymbol{x}) = B \begin{cases} \frac{G_c}{2\ell}\left(1 - \frac{d(\boldsymbol{x},l)}{\ell}\right), & \text{if } d(\boldsymbol{x},l) \le \ell \\ 0, & \text{if } d(\boldsymbol{x},l) \ge \ell \end{cases} \tag{30}$$

where, $d(\boldsymbol{x}, l)$ is the closest distance from $\boldsymbol{x}$ from the line l that represents the pre-existing crack. The scalar B has a magnitude of 10^3. Staggered scheme outlined in Section 4.2 is used to numerically solve the phase field model. One staggered iterations (if not mentioned otherwise) are used to solve the model in all the numerical examples since we used very small displacement increments. In few examples, the numerical results obtained by using the natural neighbor shape functions are compared with the finite element solution. Linear triangular elements were used in the numerical analysis using Finite Element method. All the numerical simulations were carried out on a PC with Intel(R) Xeon(R) CPU E5-2650 v4 @ 2.20 GHz and 64 GB RAM. MATLAB was used to develop the code (for both Finite Element Method and Natural Neighbor Galerkin Method). The computational time reported in this work is the time taken by the MATLAB to execute the code.

5.1. 1D Bar with a central notch

A bar with a central notch is fixed at one end and pulled at the other end with the applied displacement. The geometry and boundary conditions of the example are shown in Fig. 4. The area of cross section of the bar is assumed to be $A = 1$ mm^2 and at the notch its value it assumed to be $A = 0.25$ mm^2. The properties used are $\lambda = 121.15$ kN/mm^2, $\mu = 80.77$ kN/mm^2, and $G_c = 0.0027$ kN/mm. The displacement is applied at the end of the bar in increments of $\Delta u = 10^{-5}$ mm. The damage profile when the bar fails completely is shown in Fig. 5a for different values of the length scale parameter ℓ. The load displacement plots for different length scales ℓ is shown in Fig. 5b. It is seen that with the decrease in the length scale, there is an increase in the failure load and failure displacement. Borden et al. [52] derived an expression of critical tensile stress that 1D bar can sustain and is given as

$$\sigma_c = \frac{9}{16}\sqrt{\frac{EG_c}{3\ell}} \tag{31}$$

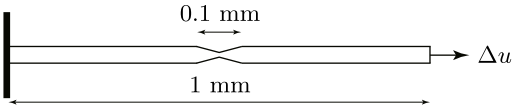

Fig. 4. Geometry and boundary conditions of the 1D bar with a center notch.

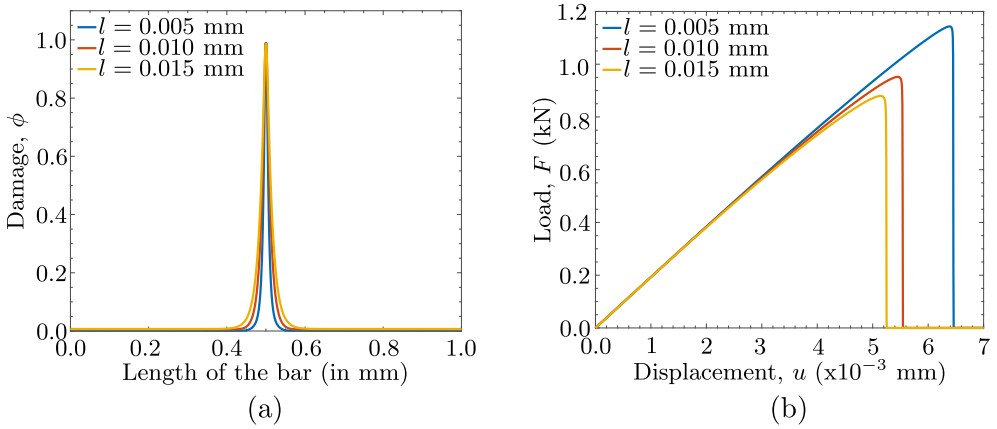

Fig. 5. (a) Damage profile of the 1D bar for different values of length scale parameter ℓ at the failure load. (b) Load-Deflection curves for the 1D bar for the different values of length scale ℓ..

where, E is the Young's modulus of the material. This expression confirms the observation that failure load increases with the decrease in the length scale parameter ℓ. This observation leads to the conclusion that the length scale ℓ should be seen as a material parameter. Therefore, the length scale ℓ should be chosen based on the experimental data. The critical tensile stress σ_c, Young's modulus E and Griffith's critical fracture energy G_c can be determined for a material using experiments. With all these values known, the length scale parameter can be calculated using Eq. (31). It should also be noted that when $\ell \to 0$, the critical stress becomes infinite which is in accordance with the properties of Griffith's theory (i.e. crack nucleates at stress singularities). The effect of length scale has been studied in detail in the works of Pham et al. [25] and Amor et al. [72]. In one dimension, natural neighbor interpolation is same as linear finite elements [70]. The natural neighbor shape functions in one dimension are given as

$$\Lambda_I = \frac{x_{I+1} - x}{x_{I+1} - x_I} \quad \text{and} \quad \Lambda_{I+1} = \frac{x - x_I}{x_{I+1} - x_I} \tag{32}$$

where, x_I and x_{I+1} are the coordinates of two adjacent nodes. Therefore, solutions obtained using finite element interpolants and natural neighbor interpolants will be the same.

5.2. Plate with an embedded center crack

In this example, we consider a square plate with a sharp crack Γ embedded in its center. The geometry and the boundary conditions considered are depicted in Fig. 6. In order to capture the discrete crack (i.e., when the length scale becomes zero), we need to discretize the body with sharp crack with infinite number of elements (nodal spacing $h = 0$) which is impossible. This example is to study the role of the length scale ℓ and the nodal spacing h (element size in the case of FEM) in the numerical computation of regularized crack topology Γ_ℓ. It is also to demonstrate the regularization of a sharp crack. The contour plots of the regularized crack topology $\phi(\boldsymbol{x})$ for different length scales are shown in Fig. 7 and it is the pictorial representation for Γ-convergence (i.e., $\Gamma_\ell \to \Gamma$ when $\ell \to 0$).

For modeling with very small length scales ℓ, there is a need for extremely fine meshes to resolve the regularized crack surface which results in higher computational cost. It should be noted the need for finer mesh only arises in the region where crack is expected to propagate. It is shown that, in Finite Element Method, an element size

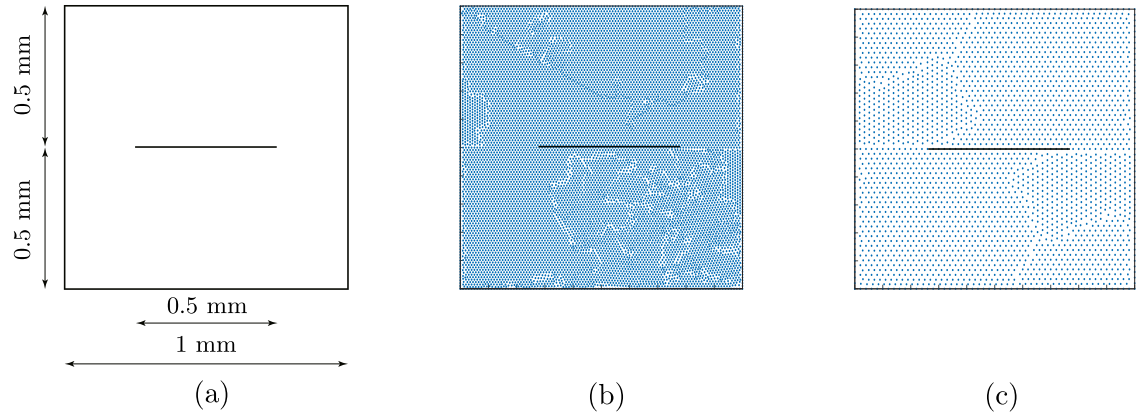

Fig. 6. Plate with an embedded center crack. (a) Geometry and boundary conditions, (b) nodal distribution with 11617 nodes for the nodal spacing of $h = 0.01$ mm, and (c) nodal distribution with 2921 nodes for the nodal spacing of $h = 0.02$ mm.

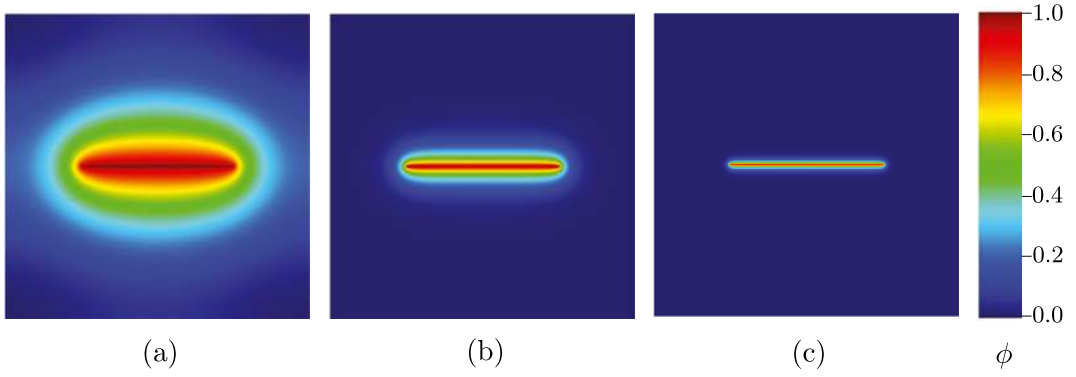

Fig. 7. Regularized crack surfaces for different length scales (a) $l = 0.32$ mm, (b) $l = 0.04$ mm, and (c) $l = 0.01$ mm obtained with a nodal spacing of $h = 0.005$ mm.

of $h < (\ell/2)$ is needed to resolve the regularized crack surface [54]. Here, we show that, with natural neighbor interpolants, a nodal spacing of $h < \ell$ is sufficient to resolve the regularized crack surface even closer to the crack. Also, the use of natural neighbor shape functions also results in better accuracy. This reduces the computational effort needed to numerically implement the phase field model. In Fig. 8, three fixed nodal spacing of $h = 0.025$ mm, $h = 0.010$ mm, and $h = 0.005$ mm were used. The length scale was varied and the regularized crack surface Γ_ℓ was numerically computed. It can be seen that the ratio (Γ/Γ_ℓ) is maximum and closer to one at $(\ell/h) = 1$ in the case of Natural Neighbor Galerkin Method. Also, a desired condition $\Gamma_\ell \simeq \Gamma$ is achieved better with Natural Element Galerkin Method. To resolve a length scale $\ell = 0.02$ mm, one needs a nodal spacing of $h = 0.01$ mm with finite element method and $h = 0.02$ mm with Natural Neighbor Galerkin approach. The nodal distribution for these two spacings are shown in Fig. 6b and 6c, respectively. The finite element simulation for $h = 0.01$ mm needed a computational time of 1.055 s, whereas, the numerical simulation with natural neighbor interpolants needed a computational time of 1.012 s. Though the computational time is almost same, only fewer nodes are required to resolve a length scale ℓ with natural neighbor Galerkin method compared to finite element method.

The comparison of accuracy of the regularized crack topology was shown in Fig. 8 in the manuscript for different fixed nodal spacings. This also includes a coarse discretization. In all the cases of nodal spacing, the curve corresponding to Natural Neighbor Galerkin Method peaked at $\ell/h = 1$ and the curve corresponding to FEM peaked at $\ell/h = 2$. We infer from this that, to resolve a length scale ℓ, one needs $h = 0.5\ell$ with Finite Element Method and $h = \ell$ with Natural Neighbor Galerkin Method. This means that fewer nodes are needed with Natural Neighbor Galerkin Method, which results in lower computational effort. This also indicates that the rates at which

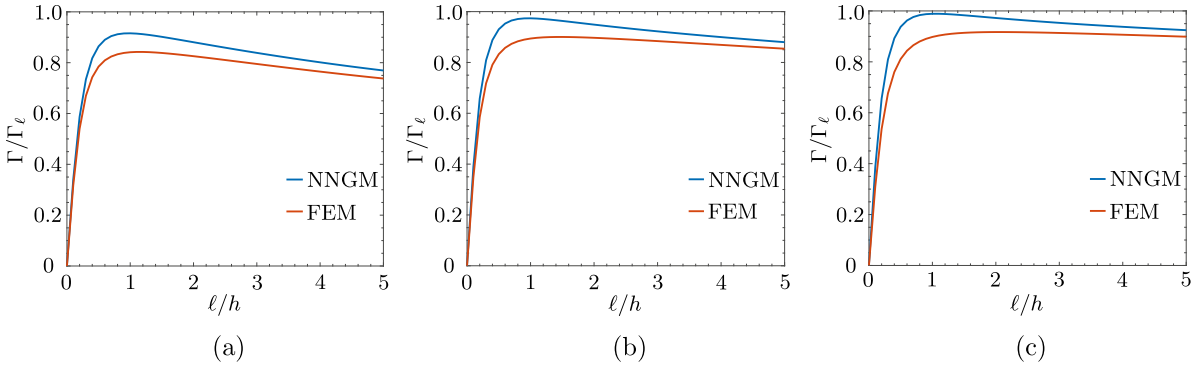

Fig. 8. Comparison of accuracy of the regularized crack topology for a fixed nodal spacing of (a) $h = 0.025$ mm, (b) $h = 0.010$ mm, and (c) $h = 0.005$ mm.

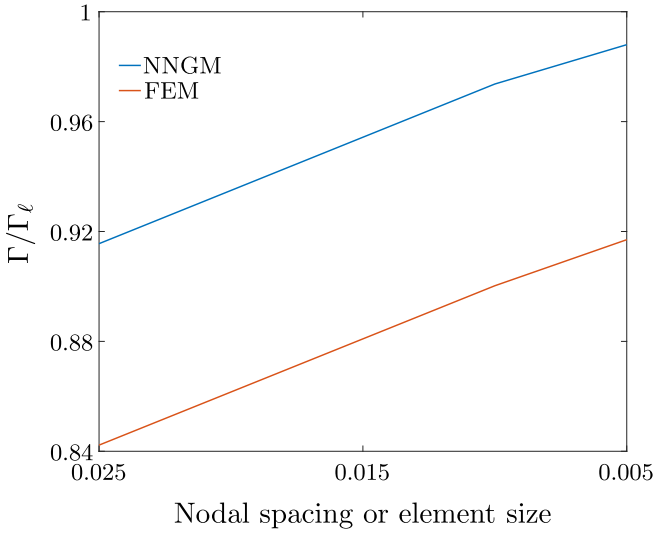

Fig. 9. Nodal spacing h versus the ratio Γ/Γ_ℓ.

the solution converge in Natural Neighbor Galerkin method is much faster than in FEM. The peak values of Γ/Γ_ℓ versus the nodal spacing for both the cases are shown in Fig. 9:

It is observed that the accuracy with Natural Neighbor Galerkin Method is better when compared with the Finite Element Method for any nodal spacing.

5.3. Edge notched specimen under tension

A square plate with a horizontal edge notch is considered for this example. The geometry and boundary conditions are shown in Fig. 10. The upper boundary of the plate is subjected to a vertical displacement Δu. The material parameters are chosen as $\lambda = 121.15$ kN/mm^2, $\mu = 80.77$ kN/mm^2 and $G_c = 0.0027$ kN/mm. The state of plane strain is assumed. Two values of the length scale parameter are considered for the analysis: $\ell = 0.0075$ mm and $\ell = 0.015$ mm. For the case of $\ell = 0.015$ mm and $\ell = 0.0075$ mm, the model is discretized using 4982 nodes and 16184nodes respectively. Refined mesh is used where the crack is expected to propagate. The numerical computation are carried out for the monotonic displacement increments of $\Delta u = 10^{-5}$ mm. The pre-existing notch is induced numerically using Eq. (30).

As expected, the crack nucleates at the tip of the pre-existing notch and propagates horizontally. The crack pattern for the length scale of $\ell = 0.0075$ mm at various displacements are shown in Fig. 11. The load–displacement curve

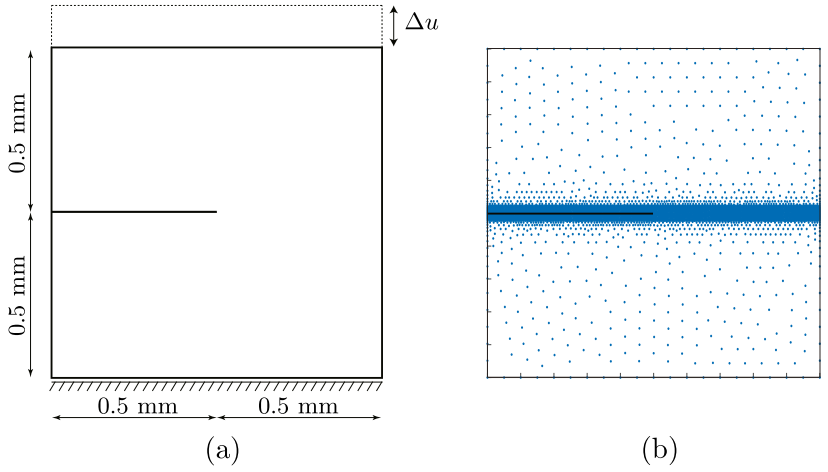

Fig. 10. Edge notched specimen under tension. (a) Geometry and boundary conditions and (b) the nodal distribution with 4982 nodes.

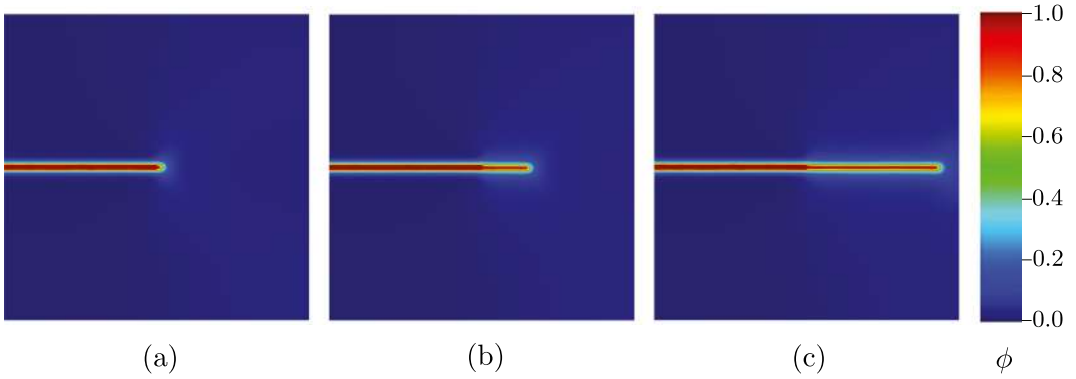

Fig. 11. Crack pattern of the edge notched specimen under tension at the displacement of (a) $u = 0.0052$ mm, (b) $u = 0.0055$ mm, and (c) $u = 0.0059$ mm for the length scale of $l = 0.0075$ mm.

obtained using finite element method and Natural Neighbor Galerkin Method for the length scale of $\ell = 0.015$ mm is shown in Fig. 12. At each time step, eight staggered iterations were carried out to obtain these curves. It is seen that the load–displacement curves obtained by both numerical tool match perfectly. Also, these results match well with those reported in the works of Miehe et al. [53] and Rabczuk et al. [73]. The effect of the number of staggered iterations and the viscosity parameter on the load displacement curve are shown in Fig. 13a and 13b, respectively. The computational time taken for this simulation for $l = 0.0075$ mm was 522 min and that obtained from standard FEM is 295 min.

Three numerical simulations were carried out for edge notched specimen under tension with three ℓ/h (same ℓ in all cases) ratios with both Natural Neighbor Galerkin Method and Finite Element Method and the load displacement plot for these cases are shown in Fig. 14:

In Fig. 14(b), it can be seen that, for the case of $\ell/h = 1$ with Finite Element Method, the load deflection curve does not converge. Whereas in Fig. 14(a), with Natural Neighbor Galerkin Method, even with $\ell/h = 1$, the load deflection curve matches with the plots of higher ℓ/h. This observation reiterates the conclusion drawn from previous example, i.e., with Natural Neighbor Galerkin Method, $h = \ell$ is enough to resolve a length scale ℓ. This results in the better convergence characteristics with coarser discretizations in Natural Neighbor Galerkin Method than those obtained from Finite Element Method. This may be attributed to the smooth (C^∞ everywhere and C^0 at nodes) and inherently nonlocal (dynamic natural neighbor based computation of compact support) approximants in Natural Neighbor Galerkin Method. The computational time required for the simulations mentioned above are tabulated as shown in Table 1.

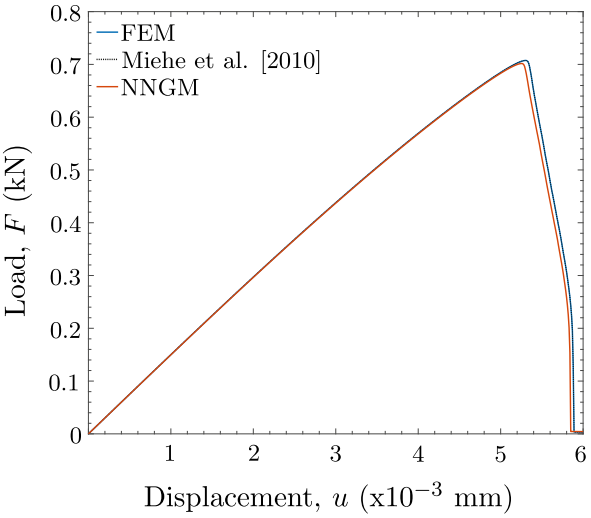

Fig. 12. Load-Deflection curves of the edge notched specimen under tension for the length scale of $\ell = 0.015$ mm.

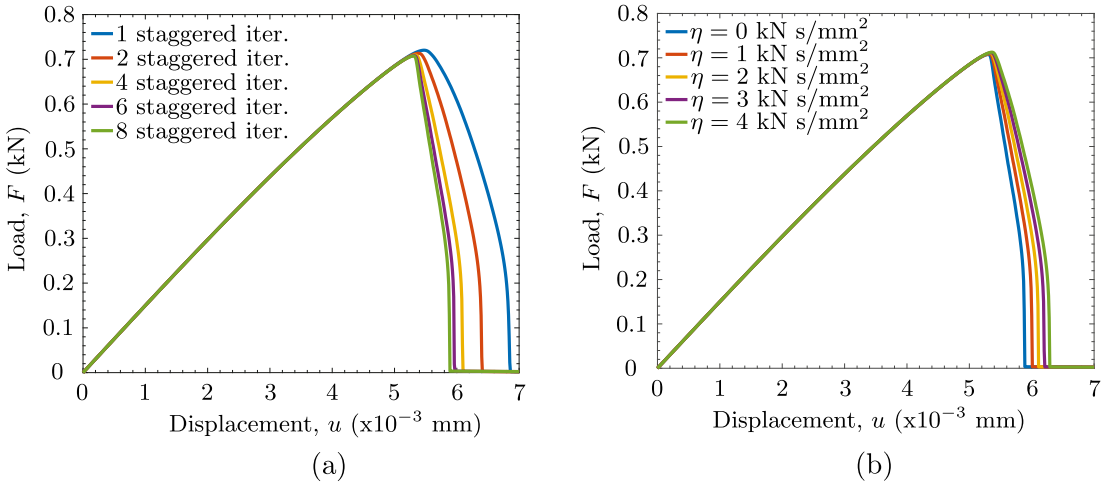

Fig. 13. Load-Deflection curves for the edge notched specimen under tension for (a) different number for staggered iterations and (b) different values of viscosity parameter η.

Table 1
Computational time (in minutes) taken to execute the phase field MATLAB code developed for Natural Neighbor Galerkin Method and Finite Element Method for different ℓ/h ratios.

ℓ/h	NNGM	FEM
1	133	82
2	522	295
3	1262	820

It is observed that the computational time required with NNGM is higher than FEM for the same discretization (same ℓ/h ratio). However, we have established in the Regularization example (Plate with an embedded center crack) that FEM and Natural Neighbor Galerkin method needs $h = 0.5\ell$ and $h = \ell$, respectively to resolve the length scale ℓ. In this case, FEM needed 295 minutes for $\ell/h = 2$ and Natural Neighbor Galerkin method needed 133 minutes for $\ell/h = 1$. Thus, from the perspective of convergence characteristics and accuracy, for a given fixed

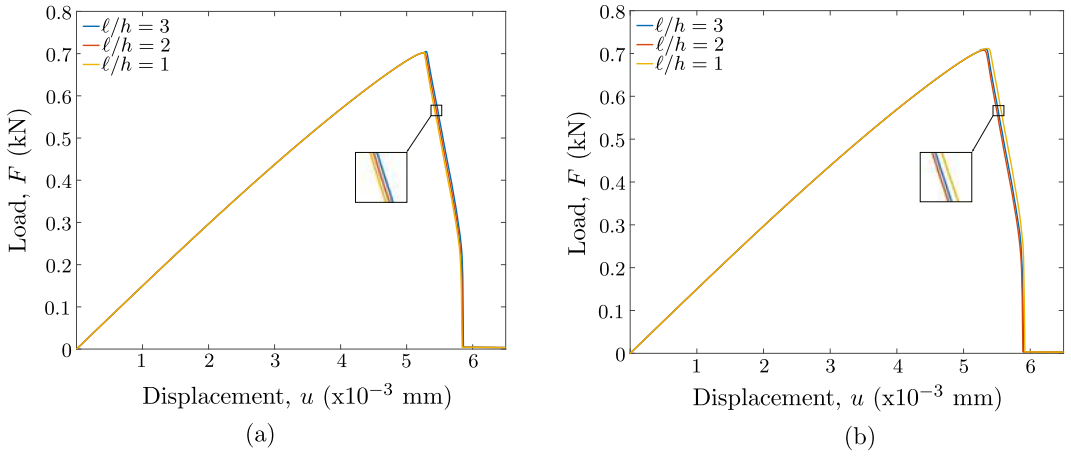

Fig. 14. Load-Deflection curves for edge notched specimen under tension for different ℓ/h ratios: Results obtained with (a) Natural Neighbor Galerkin Method and (b) Finite Element Method.

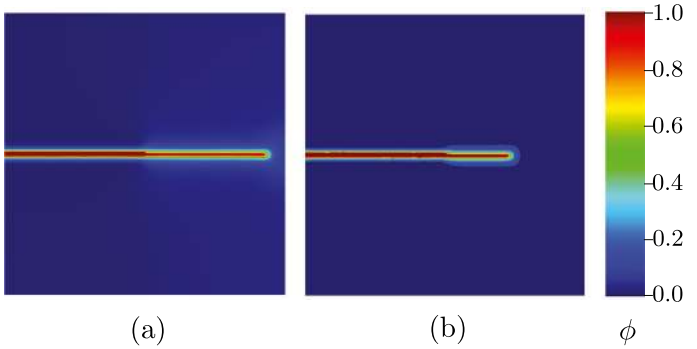

Fig. 15. Crack pattern of the edge notched specimen under tension at the displacement of $u = 0.0059$ mm for the length scale of $l = 0.0075$ mm obtained with (a) Finite Element Method with $\ell/h = 2$ and (b) Natural Neighbor Galerkin Method with $\ell/h = 1$.

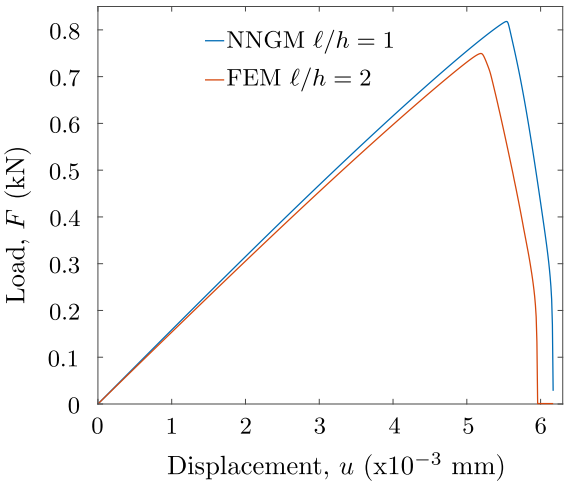

Fig. 16. Load-Deflection curves of the edge notched specimen under tension for the length scale of $\ell = 0.0075$ mm obtained with Finite Element Method with $\ell/h = 2$ and Natural Neighbor Galerkin Method with $\ell/h = 1$.

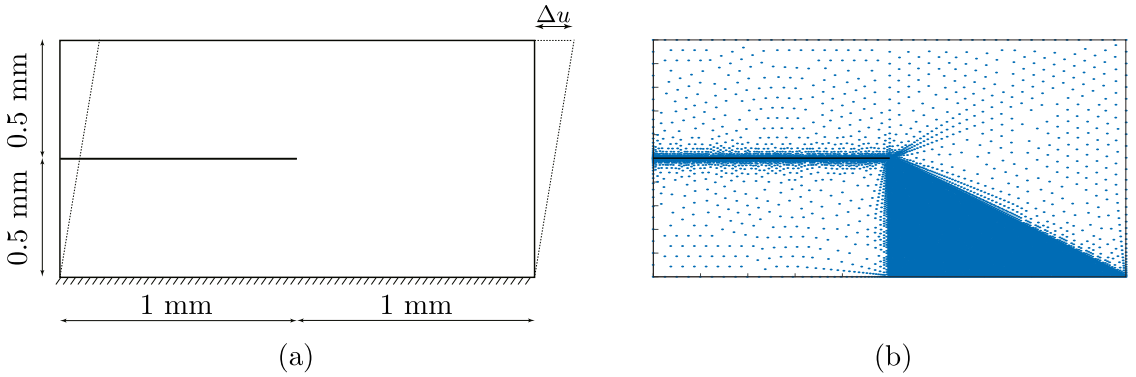

Fig. 17. Edge notched specimen under shear. (a) Geometry and boundary conditions and (b) the nodal distribution with 19887 nodes.

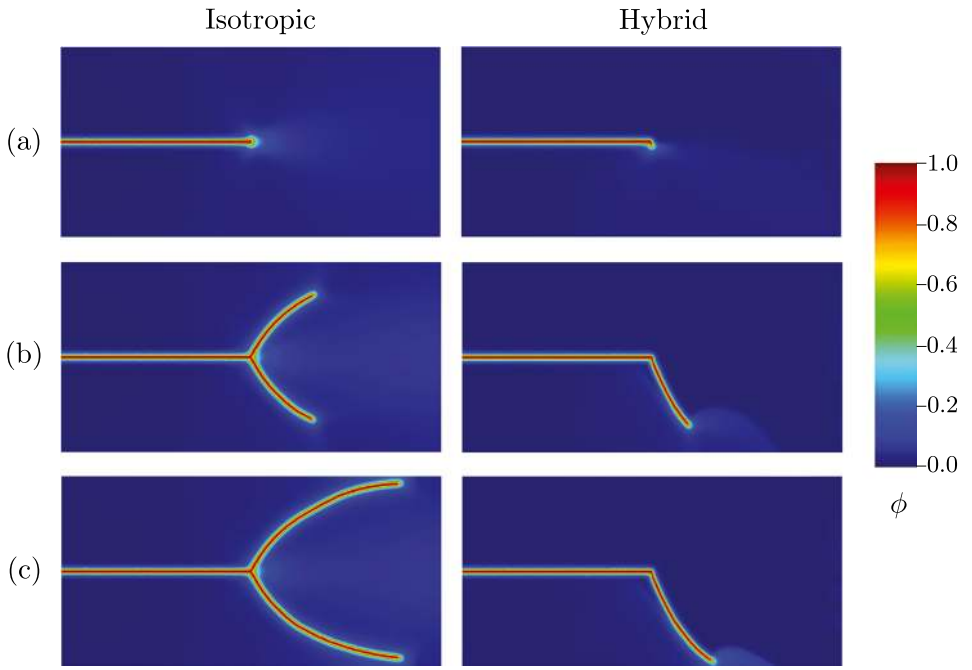

Fig. 18. Crack pattern of the edge notched specimen under shear at the displacement of (a) $u = 0.01$ mm, (b) $u = 0.013$ mm, and (c) $u = 0.016$ mm for the length scale of $l = 0.01$ mm.

mesh the Natural Element Galerkin Method is better than FEM. A comparison of the NNGM results with $\ell/h = 1$ and FEM with $\ell/h = 2$ is made. A more detailed study in to performance of NNGM with $\ell/h = 1$ and FEM with $\ell/h = 2$ was made by plotting of crack paths for this length scale. The results are shown in Figs. 15 and 16 for the edge notch specimen under tension. Fig. 15 shows the crack pattern of the edge notched specimen under tension at the displacement of $u = 0.0059$ mm for the length scale of $l = 0.0075$ mm obtained with (a) Finite Element Method with $\ell/h = 2$ and (b) Natural Neighbor Galerkin Method with $\ell/h = 1$, both showing similar results. Fig. 16 shows the Load-Deflection curves of the edge notched specimen under tension for the length scale of $\ell = 0.0075$ mm obtained with Finite Element Method with $\ell/h = 2$ and Natural Neighbor Galerkin Method with $\ell/h = 1$. Its is observed that the NNGM is computationally more efficient than the FEM.

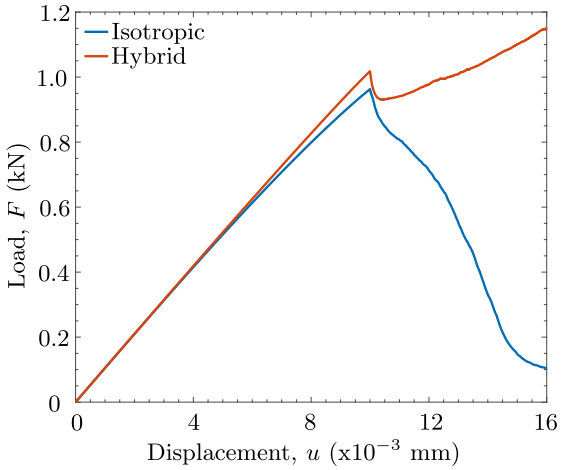

Fig. 19. Load-Deflection curves of the edge notched specimen under shear for the length scale of $\ell = 0.005$ mm.

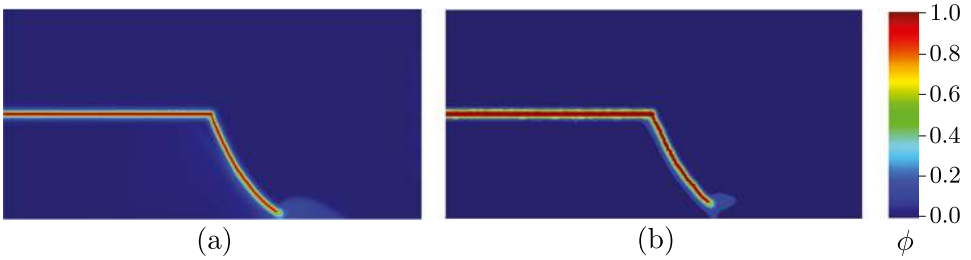

Fig. 20. Crack pattern of the edge notched specimen under shear at the displacement of $u = 0.016$ mm for the length scale of $l = 0.01$ mm obtained with (a) Finite Element Method with $\ell/h = 2$ and (b) Natural Neighbor Galerkin Method with $\ell/h = 1$.

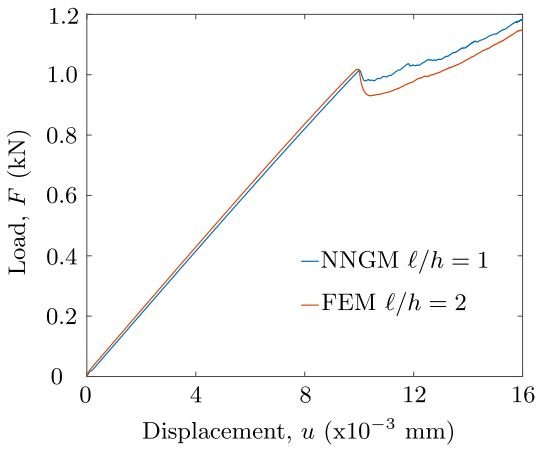

Fig. 21. Load-Deflection curves of the edge notched specimen under shear for the length scale of $\ell = 0.01$ mm obtained with Finite Element Method with $\ell/h = 2$ and Natural Neighbor Galerkin Method with $\ell/h = 1$.

5.4. Edge notched specimen under shear

A rectangular plate with an edge notch is considered for this example. The geometry and boundary conditions are shown in Fig. 17. The material parameters are chosen as $\lambda = 121.15$ kN/mm^2, $\mu = 80.77$ kN/mm^2 and $G_c = 0.0027$ kN/mm. The state of plane strain is assumed. The plate is discretized using 19887 nodes and a length

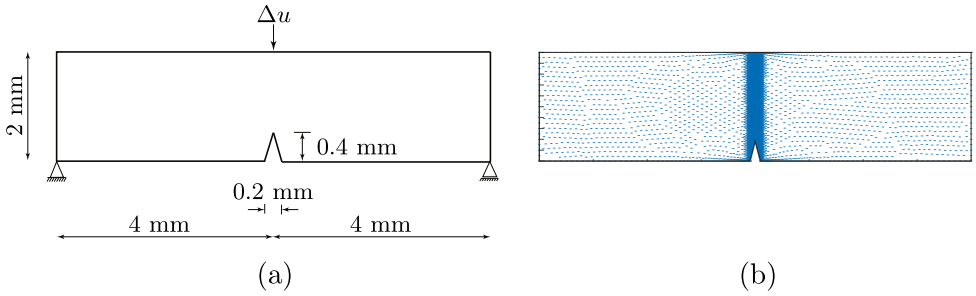

Fig. 22. Symmetric three point bending test. (a) Geometry and boundary conditions and (b) the nodal distribution with 4894 nodes.

scale of $\ell = 0.01$ mm is used. Refined mesh is used where the crack is expected to propagate. The computation is carried out with the displacement increment of $\Delta u = 10^{-4}$ mm in the first 100 time steps and $\Delta u = 2\times10^{-6}$ mm in the subsequent time steps. The simulation was carried out for the isotropic case (without the energy decomposition into tensile and compressive parts). The consequence is that crack growth can occur also under compressive state of stress which is an unrealistic response. The results from the isotropic model and hybrid model are shown in Fig. 18. This is to demonstrate the necessity of the energy decomposition such that only tensile part of the elastic energy drives the evolution of the phase field. The load deflection curves for both the isotropic and hybrid cases are presented in Fig. 19. The computational time taken for this simulation with $l = 0.01$ mm for the hybrid case was 4608 min, while that obtained from FEM was 2908 min.

A comparison of the NNGM results with $\ell/h = 1$ and FEM with $\ell/h = 2$ is made. A more detailed study in to performance of NNGM with $\ell/h = 1$ and FEM with $\ell/h = 2$ was made by plotting of crack paths for this length scale. The results are shown in Figs. 20 and 21 for the edge notch specimen under shear. Fig. 20 shows the crack pattern of the edge notched specimen under shear at the displacement of $u = 0.016$ mm for the length scale of $l = 0.01$ mm obtained with (a) Finite Element Method with $\ell/h = 2$ and (b) Natural Neighbor Galerkin Method with $\ell/h = 1$. Both the methods are more or less giving similar crack paths. Fig. 21 shows the load deflection diagram clearly indicating that NNGM is still a flexible discretization even with $\ell/h = 1$.

5.5. Symmetric three point bending test

This example considers the three point bending test of a notched beam. The geometry and boundary conditions of the problem are depicted in Fig. 22. The material parameters are chosen as $\lambda = 12$ kN/mm^2, $\mu = 8$ kN/mm^2 and $G_c = 5 \times 10^{-4}$ kN/mm. The beam is discretized using 4894 nodes and a length scale of $\ell = 0.03$ mm is used. Refined mesh is used where the crack is expected to propagate. The computation is carried out with the displacement increment of $\Delta u = 10^{-4}$ mm in the first 360 time steps, $\Delta u = 10^{-6}$ in the next 24000 time steps and $\Delta u = 10^{-5}$ mm in the subsequent time steps. Fig. 23 depicts the contour profile of the phase field at various displacements for the length scale of $\ell = 0.03$ mm. Fig. 24 shows the load displacement curve for the symmetric three point bending test, which matches with the curve presented in Miehe et al. [53]. The computational time taken for this simulation for $l = 0.03$ mm was 13680 min, whereas that obtained from FEM was 9216 min.

5.6. Asymmetrically notched three point bending test

This example considers the three point bending test of an asymmetrically notched beam. The geometry and boundary conditions of the problem are depicted in Fig. 25. The material parameters are chosen as $\lambda = 12$ kN/mm^2, $\mu = 8$ kN/mm^2 and $G_c = 10^{-3}$ kN/mm. The beam is discretized using 17680 nodes and a length scale of $\ell = 0.03$ mm is used. Refined mesh is used where the crack is expected to propagate. The computation is carried out with the displacement increment of $\Delta u = 4.2\times10^{-3}$ mm in the first 50 time steps, $\Delta u = 10^{-4}$ in the subsequent time steps. Fig. 26 depicts the contour profile of the phase field at various displacements for the length scale of $\ell = 0.03$ mm. The crack pattern is similar to that obtained by Bittencourt et al. [74]. Fig. 27 shows the load displacement curve for the asymmetrically notched three point bending test. The load displacement curve obtained for this numerical

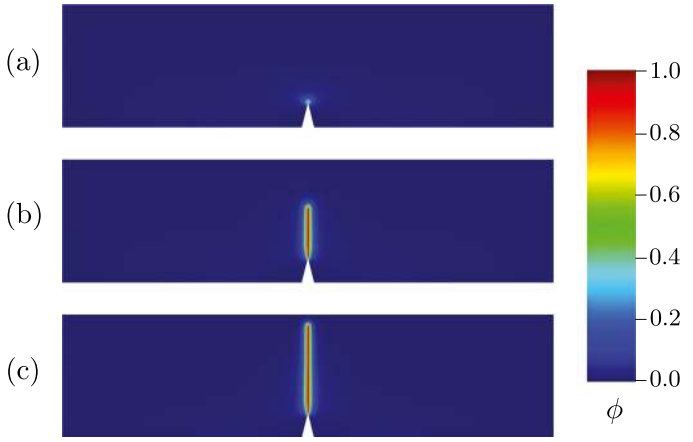

Fig. 23. Crack pattern at the displacement of (a) $u = 0.043$ mm, (b) $u = 0.044$ mm, and (c) $u = 0.1$ mm for the length scale of $l = 0.03$ mm.

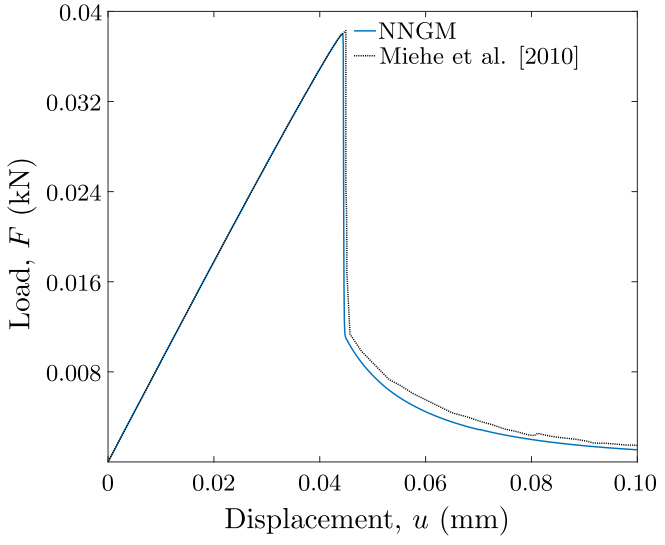

Fig. 24. Load-Deflection curve for the symmetric three point bending test.

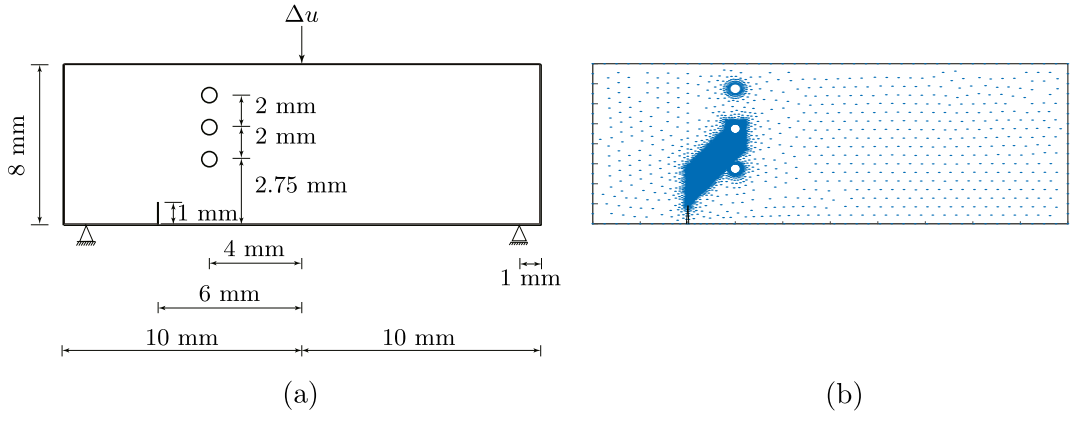

Fig. 25. Asymmetrically notched three point bending test. (a) Geometry and boundary conditions and (b) the nodal distribution with 17680 nodes.

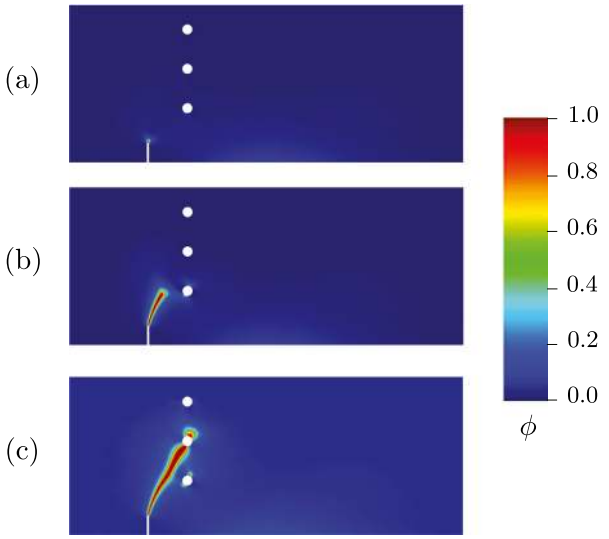

Fig. 26. Crack pattern at the displacement of (a)$u = 0.21$ mm, (b)$u = 0.215$ mm, and (c)$u = 0.2175$ mm for the length scale of $l = 0.03$ mm.

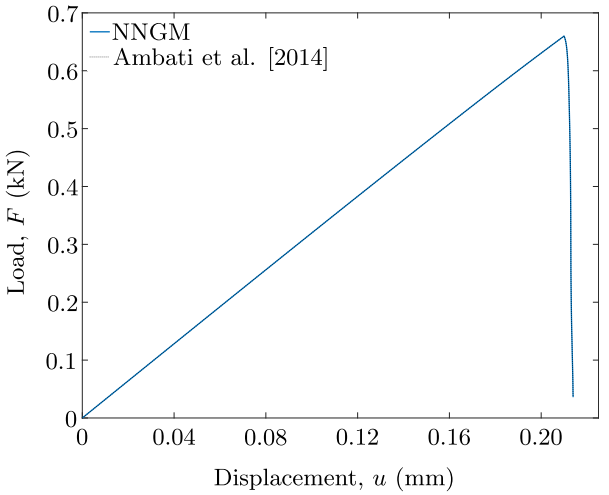

Fig. 27. Load-Deflection curve for the asymmetrically notched three point bending test.

example matches with the result presented in Ambati et al. [50]. The computational time taken for this simulation for $l = 0.03$ mm was 2736 min, whereas that obtained from FEM was 1728 min.

For all the numerical examples, $\ell/h = 2$ was considered for the analysis with both Natural Element Galerkin Method and Finite Element Method. The interest was to compare the FEM results obtained for an adequately refined good mesh for both FEM and NNGM. A more detailed study in to performance of NNGM $\ell/h = 1$ and plotting of crack paths for this length scale is a future study. The computational time need for NNGM is higher than Finite Element Method. The computational times taken for the simulation are tabulated in Table 2.

6. Conclusions

In the present work we have demonstrated the use of natural neighbor Galerkin method for phase field modeling of quasi-brittle fracture problems. The use of natural neighbors to dynamically decide the compact support at a nodal point makes it truly mesh free and nonlocal. The method uses smooth non-polynomial type Sibson interpolants,

Table 2
Computational time (in minutes) taken to execute the phase field MATLAB code.

Example	NNGM	FEM
Edge notched specimen under shear (Hybrid)	4608	2980
Symmetric three point bending test	13680	9216
Asymmetrically notched three point bending test	2736	1728

which are C^0 at a given node and C^1 everywhere else. This allows accurate capture of the interface region in a phase field model with only few number of nodes. For a given accuracy, there is a marginal improvement in the computational time. Only fewer nodes are required to resolve a length scale ℓ with natural neighbor Galerkin method compared to the finite element method.

Declaration of competing interest

The authors declare that they have no known competing financial interests or personal relationships that could have appeared to influence the work reported in this paper.

References

[1] A.A. Griffith, The phenomena of rupture and flow in solids, Phil. Trans. R. Soc. A 221 (1921) 163–198.
[2] G.R. Irwin, Analysis of stresses and strains near the end of a crack traversing a plate, J. Appl. Mech. 24 (1957) 361–364.
[3] J.R. Rice, A path independent integral and the approximate analysis of strain concentrations by notches and cracks, J. Appl. Mech. ASME 35 (1968) 379–386.
[4] G. Pijaudier-Cabot, Z.P. Baant, Nonlocal damage theory, J. Eng. Mech. 118(10) (1987) 1512–1533.
[5] L.M. Kachanov, Time of rupture process under creep conditions, Izv. Sib. Otd. Akad. Nauk SSSR Ser. Tekh. Nauk 8 (1958) 26–31.
[6] G.J. Barenblatt, The formation of equilibrium cracks during brittle fracture, general ideas and hypotheses- axially symmetric cracks, J. Appl. Math. Mech. 23 (1959) 622–636.
[7] G.J. Barenblatt, The mathematical theory of equilibrium of cracks in brittle fracture, Adv. Appl. Fract. 7 (1962) 55–129.
[8] T. Belytschko, J. Fish, B.E. Engelmann, A finite element with embedded localization zones, Comput. Methods Appl. Mech. Eng. 70(1) (1988) 59–89.
[9] M. Jirásek., Nonlocal theories in continuum mechanics, Acta Polytech. 44 (2004) 16–34.
[10] R. De Borst, L.J. Sluys, H.B. Mühlhaus, Fundamental issues in finite element analysis of localization of deformation, Eng. Comput. 10 (1993) 99–121.
[11] A. Hillerborg, M. Modeer, P. Petersson, Analysis of crack formation and crack growth in concrete by means of fracture mechanics and finite elements, Cement Concr. Res. 6 (1976) 773–781.
[12] J.C. Simo, J. Oliver, F. Armero, An analysis of strong discontinuities induced by strain softening in rate independent inelastic solids, Comput. Mech. 12(5) (1993) 277–296.
[13] J. Oliver, Modeling strong discontinuities in solid mechanics via strain softening constitutive equations part I and II, Int. J. Numer. Methods Eng. 39 (1996) 3575–3623.
[14] F. Armero, K. Garikipati, An analysis of strong discontinuities in multiplicative finite strain plasticity and their relation with numerical simulation of strain localization in solids, Int. J. Solids Struct. 33(20-22) (1996) 2863–2885.
[15] M. Jirasek, T. Zimmermann, Embedded crack model: I basic formulation, Int. J. Numer. Methods Eng. 50 (2001) 1269–1290.
[16] J. Oliver, Continuum modelling of strong discontinuities in solid mechanics using damage models, Comput. Mech. 17(1-2) (1995) 49–61.
[17] A. Needleman, An analysis of decohesion along an imperrfect interface, Int. J. Fract. 42 (1990) 21–40.
[18] Z.P. Bazant, B.H. Oh, Crack band theory for fracture of concrete, Mater. Struct. 16 (1983) 155–177.
[19] J. Rots, Computational Modeling of Concrete Fracture (Ph.D. thesis), Delft University of Technology, 1988.
[20] B. Patzak, M. Jirasek, Process zone resolution by extended finite elements, Eng. Fract. Mech. 70 (2003) 957–977.
[21] S. Murakami, Continuum Damage Mechanics, Springer, New York, 2012.
[22] Z.P. Bažant, G. Pijaudier-Cabot, Nonlocal continuum damage, localization instability and convergence, J. Appl. Mech. 55 (1988) 521–539.
[23] R. Peerlings, M. Geers, R.D. Borst, W. Brekelmans, J.D. Vree, Gradient enhanced damage for quasi brittle materials, Internat. J. Numer. Methods Engrg. 39 (1996) 3391‘–3403.
[24] R. Peerlings, M. Geers, R. de Borst, W. Brekelmans, A critical comparison of nonlocal and gradient enhanced softening continua, Int. J. Solids Struct. 38 (2001) 7723–7746.
[25] K. Pham, H. Amor, J.-J. Marigo, C. Maurini, Gradient damage models and their use to approximate brittle fracture, Int. J. Damage Mech. 20 (2011) 618–655.
[26] M. Frémond, B. Nedjar, Damage, gradient of damage and principle of virtual power, Int. J. Solids Struct. 33(8) (1996) 1083–1103.

[27] G. Pijaudier-Cabot, N. Burlion, Damage and localization in elastic materials with voids, Mech. Cohesive Frictional Mater. 1 (1996) 129–144.
[28] E. Lorentz, A nonlocal damage model for plain concrete consistent with cohesive fracture, Int. J. Fract. 207 (2017) 123–159.
[29] P. Steinmann, C. Miehe, E. Stein, Comparison of different finite deformation inelastic damage models within multiplicative elastoplasticity for ductile materials, Comput. Mech. 13(6) (1994) 458–474.
[30] P. Steinmann, Formulation and computation of geometrically nonlinear gradient damage, Internat. J. Numer. Methods Engrg. 46(5) (1999) 757–779.
[31] A. Javili, P. Steinmann, Geometrically nonlinear higher - gradient elasticity with energetic boundaries, J. Mech. Phys. Solids 61(12) (2013) 2381–2401.
[32] S. Sarkar, I.V. Singh, B.K. Mishra, A.S. Shedbale, L.H. Poh, A comparative study and ABAQUS implementation of conventional and localizing gradient enhanced damage models, Finite Elem. Anal. Des. 160 (2019) 1–31.
[33] Z. Wang, L.H. Poh, A homogenized localizing gradient damage model with micro inertia effect, J. Mech. Phys. Solids 116 (2018) 370–390.
[34] V.B. Pandey, I.V. Singh, B.K. Mishra, S. Ahmad, A. Venugopal Rao, A new framework based on continuum damage mechanics and XFEM for high cycle fatigue crack growth simulations, Eng. Fract. Mech. 206 (2019) 172–200.
[35] P. Areias, T. Rabczuk, Finite strain fracture of plates and shells with configurational forces and edge rotations, Internat. J. Numer. Methods Engrg. 94 (2013) 1099–1122.
[36] M.J. Borden, T.J.R. Hughes, C.M. Landis, A. Anvari, I.J. Lee, A phase-field formulation for fracture in ductile materials: Finite deformation balance law derivation, plastic degradation, and stress triaxiality effects, Comput. Methods Appl. Mech. Engrg. 312 (2016) 130–166.
[37] M. Ambati, L. De Lorenzis, Phase-field modeling of brittle and ductile fracture in shells with isogeometric NURBS-based solid-shell elements, Comput. Methods Appl. Mech. Engrg. 312 (2016) 351–373.
[38] S. Teichtmeister, D. Kienle, F. Aldakheel, M.A. Keip, Phase field modeling of fracture in anisotropic brittle solids, Int. J. Non-Linear Mech. 97 (2017) 1–21.
[39] R. Alessi, M. Ambati, T. Gerasimov, S. Vidoli, L. De Lorenzis, Comparison of phase-field models of fracture coupled with plasticity, Adv. Comput. Plast. 46 (2018) 1–21.
[40] T.K. Mandal, V.P. Nguyen, A. Heidarpour, Phase field and gradient enhanced damage models for quasi-brittle failure: A numerical comparative study, Eng. Fract. Mech. 207 (2019) 48–67.
[41] E. Tanné, T. Li, B. Bourdin, J.J. Marigo, C. Maurini, Crack nucleation in variational phase field models of brittle fracture, J. Mech. Phys. Solids 110 (2018) 80–99.
[42] K.H. Pham, K. Ravi-Chandar, C.M. Landis, Experimental validation of a phase field model for fracture, Int. J. Fract. 205 (2017) 83–101.
[43] P. Areias, J. Reinoso, P.P. Camanho, J. César de Sá, T. Rabczuk, Effective 2D and 3D crack propagation with local mesh refinement and the screened Poisson equation, Eng. Fract. Mech. 189 (2018) 339–360.
[44] M.A. Msekh, N.H. Cuong, G. Zi, P. Areias, X. Zhuang, T. Rabczuk, Fracture properties prediction of clay/epoxy nanocomposites with interphase zones using a phase field model, Eng. Fract. Mech. 188 (2018) 287–299.
[45] D.C. Feng, J.-Y. Wu, Phase-field regularized cohesive zone model (CZM) and size effect of concrete, Eng. Fract. Mech. 197 (2018) 66–79.
[46] J.-Y. Wu, V.P. Nguyen, A length scale insensitive phase field damage model for fracture, J. Mech. Phys. Solids 119 (2018) 20–42.
[47] J.-Y. Wu, A unified phase field theory for the mechanics of damage and quasi brittle failure in solids, J. Mech. Phys. Solids 103 (2017) 72–99.
[48] J.Y. Wu, A geometrically regularized gradient damage model with energetic equivalence, Comput. Methods Appl. Mech. Engrg. 328 (2018) 612–637.
[49] G.A. Francfort, J.J. Marigo, Revisiting brittle fracture as an energy minimization problem, J. Mech. Phys. Solids 46 (1998) 1319–1342.
[50] M. Ambati, T. Gerasimov, L. De Lorenzis, A review on phase field models of brittle fracture and a new fast hybrid formulation, Comput. Mech. 55 (2015) 383–405.
[51] C. Kuhn, T. Noll, R. Müller, On phase field modeling of ductile fracture, GAMM-Mitt. 39 (2016) 35–54.
[52] M.J. Borden, C.V. Verhoosel, M.A. Scott, T.J.R. Hughes, C.M. Landis, A phase-field description of dynamic brittle fracture, Comput. Methods Appl. Mech. Engrg. 217 (2012) 77–95.
[53] C. Miehe, M. Hofacker, F. Welschinger, A phase field model for rate-independent crack propagation: Robust algorithmic implementation based on operator splits, Comput. Methods Appl. Mech. Engrg. 199 (2010) 2765–2778.
[54] C. Miehe, F. Welschinger, M. Hofacker, Thermodynamically consistent phase-field models of fracture: Variational principles and multi-field FE implementations, Internat. J. Numer. Methods Engrg. 83 (2010) 1273–1311.
[55] S. Lee, M.F. Wheeler, T. Wick, Pressure and fluid-driven fracture propagation in porous media using an adaptive finite element phase field model, Comput. Methods Appl. Mech. Engrg. 305 (2016) 111–132.
[56] M.J. Borden, T.J.R. Hughes, C.M. Landis, C.V. Verhoosel, A higher-order phase-field model for brittle fracture: Formulation and analysis within the isogeometric analysis framework, Comput. Methods Appl. Mech. Engrg. 273 (2014) 100–118.
[57] B. Bourdin, G.A. Francfort, J.J. Marigo, Numerical experiments in revisited brittle fracture, J. Mech. Phys. Solids 48 (2000) 797–826.
[58] R. Alessi, J.J. Marigo, S. Vidoli, Gradient damage models coupled with plasticity: Variational formulation and main properties, Mech. Mater. 80(Part B) (2015) 351–367.
[59] H. Ulmer, M. Hofacker, C. Miehe, Phase field modeling of fracture in plates and shells, Proc. Appl. Math. Mech. 12 (2012) 171–172.
[60] F. Amiri, D. Millán, M. Arroyo, M. Silani, T. Rabczuk, Fourth order phase-field model for local max-ent approximants applied to crack propagation, Comput. Methods Appl. Mech. Engrg. 312 (2016) 254–275.

[61] J. Kiendl, M. Ambati, L. De Lorenzis, H. Gomez, A. Reali, Phase-field description of brittle fracture in plates and shells, Comput. Methods Appl. Mech. Engrg. 312 (2016) 374–394.
[62] R.U. Patil, B.K. Mishra, I.V. Singh, A multiscale framework based on phase field method and XFEM to simulate fracture in highly heterogeneous materials, Theor. Appl. Fract. Mech. 100 (2019) 390–415.
[63] R.U. Patil, B.K. Mishra, I.V. Singh, T.Q. Bui, A new multiscale phase field method to simulate failure in composites, Adv. Eng. Softw. 126 (2018) 9–33.
[64] R.U. Patil, B.K. Mishra, I.V. Singh, A local moving extended phase field method for failure analysis of brittle materials, Comput. Methods Appl. Mech. Engrg. 342 (2018) 674–709.
[65] Y. Shao, Q. Duan, S. Qiu., Adaptive consistent element free Galerkin method for phase field model of brittle fracture, Comput. Mech. (2019) 1–27.
[66] V. Mohammadi, M. Dehghan, Simulation of phase field Cahn hilliard and tumor growth models via a numerical scheme: Element - free Galerkin method, Comput. Methods Appl. Mech. Engrg. 345(1) (2019) 919–950.
[67] A. Braides, Approximation of Free-Discontinuity Problems, vol. 1694, Springer, Verlag Berlin Heidelberg, 1998.
[68] A. Rajagopal, P. Fischer, E. Kuhl, P. Steinmann, Natural element analysis of Cahn-hilliard phase field model, Comput. Mech. 46(3) (2010) 471–493.
[69] G.R. Balachandran, A. Rajagopal, S.M. Sivakumar, Meshfree methods based on natural neighbours and conformal mapping, Comput. Mech. 42 (2008) 885–892.
[70] N. Sukumar, B. Moran, T. Belytschko, The natural element method in solid mechanics, Internat. J. Numer. Methods Engrg. 43 (1998) 839–887.
[71] E. Cueto, N. Sukumar, B. Calvo, M. Martínez, J. Cegoñino, M. Doblaŕe, Overview and recent advances in natural neighbor Galerkin methods, Arch. Comput. Methods Eng. 10(4) (2003) 307–384.
[72] H. Amor, J.-J. Marigo, C. Maurini, Regularized formulation of the variational brittle fracture with unilateral contact: Numerical experiments, J. Mech. Phys. Solids 57 (2009) 1209–1229.
[73] S. Zhou, T. Rabczuk, X. Zhuang, Phase field modeling of quasi-static and dynamic crack propogation: COMSOL implementation and Case studies, Adv. Eng. Softw. 122 (2018) 31–49.
[74] T.N. Bittencourt, P.A. Wawrzynek, A.R. Ingraffea, J.L. Sousa, Quasi-automatic simulation of crack propagation for 2D LEFM problems, Eng. Fract. Mech. 55 (1996) 321–334.